StereoMate: A Stereological and Automated Analysis Platform for Assessing Histological Labelling in Cleared Tissue Specimens

Steven J. West, David L Bennett

21/05/2019

Nuffield Department of Clinical Neuroscience, University of Oxford, UK

Corresponding authors:

Prof DL Bennett

Tel: +44(0)1865 231512 **Email**: david.bennett@ndcn.ox.ac.uk

Fax: 01865 234 830

Dr SJ West

Email: Steven.west@ndcn.ox.ac.uk

Fax: 01865 234 830

Abstract

The recent resurgence of tissue clearing methods presents a number of challenges. Cleared tissue protocols remain refractory to complete immunofluorescence labelling, and demonstrating a reliable and accurate extraction of object-level data from the resultant images is currently unavailable in an automated and stereological manner.

These challenges are met with the StereoMate platform, consisting of a tissue clearing methodology optimised for immunofluorescence labelling, and an open-source image analysis framework, allowing development of image segmentation protocols with rigorous validation, and extraction of object-level data in an automated and stereological manner.

This platform is used to explore mouse dorsal root ganglion neurones, revealing a novel trimodal distribution to 3D DRG neurone size. Finally, its power is

demonstrated by identifying a profound loss and shift in DRG neurone size resulting from peripheral nerve injury.

In conclusion, the StereoMate platform provides a general-purpose automated stereological analysis framework to generate rich and unbiased object-level datasets from tissue structure.

Introduction

A recent interest in tissue clearing methods have resulted in the development of several new protocols, all promising to deliver high quality 3D reconstructions of nervous system tissue[1–9].

Combining these methods with standard immunohistochemical approaches, however, has proved challenging. The process of tissue clearing appears to have severe consequences for tissue antigenicity, resulting in poor, or in some cases a complete absence, of antibody labelling[10]. With the current best approach for cleared tissue immunohistochemistry[4,8], it is recommended to check whether antigenciity is sufficiently well maintained following the initial lipid elution with different antigens.

Developing a protocol which both enables deep tissue imaging for 3D reconstructions and retains antigenicity for delivering high quality histological signal is therefore a key challenge in bringing tissue clearing methods to the fore in immunohistochemical studies.

A further challenge with tissue clearing methodologies is performing appropriate image analysis methods to the deluge of data that tissue clearing experiments produce, hampering even quite basic image analysis. A long history in histological analysis of tissue has resulted in the development of the rigorous analysis principles embodied by stereology[11,12]. Ideally, any image analysis procedure performed on 3D reconstructions will contain these principles, to ensure an unbiased and precise measure of reconstructed biological objects.

This paper describes the StereoMate platform, a pipeline, consisting of tissue clearing and immunohistochemical labelling protocols, and an automated stereological image analysis framework. The platform is applied here to tissues derived from a mouse model of peripheral nerve injury, a common cause of neuropathic pain[13]. This work reveals the profound and potentially permanent impact of peripheral nerve injury on these structures, which has important implications for the long-term consequences of neuropathic pain due to traumatic nerve injury, but potentially other causes.

Methods

Animals

Mice derived from the Advillin-eGFP line from GENSAT were used in this study. All animal experiments were were performed in accordance with the European Community directive 86/609/EC and the UK Animals (Scientific Procedures) Act 1986.

Surgery, Perfusion, Dissection

Animals were randomly allocated to receive SNI (4M/4F) or SHAM (3M/3F) surgery using aseptic technique, as previously described[14]. Briefly, animals were anaesthetised and the left sciatic nerve exposed. The common peroneal and tibial branches were ligated and transected (SNI), or no nerve manipulation was performed (SHAM), and the surgical site sealed with sutures. Animals received 50mg/kg remifentanyl as post-surgical analgesic and were routinely monitored for 6 weeks post surgery.

Animals were terminally anaesthetised and caridally perfused with PBS followed by 4% PFA, and whole L4 DRGs were carefully dissected, ensuring to retain both the dorsal and spinal root. Tissue was post-fixed for 24 hours at room temperature in the same fixitive. Tissue was washed in PBS and stored at -80 in CI-VM1[15].

Clearing and Immunohistochemistry

Tissue clearing was performed by dehydrating in a gradient of 1-propanol containing 0.3% tirethylamine (30, 50, 75, 90, 95, 100, 100%), and washed in this solution at 37C for 24 hours. Tissue was rehydrated into PBS, and antibody labelling was performed with anti-TDP43 (ab133547, abcam) 1:100 dilution at 37C for 7 days. Tissue was washed for 24 hours in buffer, and incubated in anti-rabiit Cy3 conjugated secondary antibody (711-165-152, JIR) 1:500 dilution at 37C for 7 days. Tissue was washed for 24 hours in buffer, dehydrated in 1-propanol containing 0.3% triethylamine, and mounted in BABB (benzyl alcohol, benzyl benzoate, 1:2 ratio) containing 0.3% triethylamine on glass slides with rubber silicone spacers. Tissue was secured with a No 0 coverslip for confocal imaging.

Confocal Microscopy

Confocal imaging was performed on a Zeiss LSM 700 confocal microscope. The Zeiss Objective LD LCI Plan-Apochromat 63x/1.2 Imm Corr DIC objective was used for imaging, with the correction collar set to oil and zeiss objective oil used for immersion. With the reduced coverslip thickness, this objective provides approximately 550um working distance, sufficient for whole DRG reconstruction.

Images were acquired at 1um resolution in XYZ. The laser and gain was adjusted to give optimal signal throughout the Z stack, with a gradient set to increase laser and

gain marginally through Z for even signal. A tile scan and Z stack was taken to capture the entire DRG within one image.

Image Analysis

The StereoMate ImageJ plugin suite was used for assessing wholemount DRG confocal image stacks, as described in the paper, and is freely available on github (https://github.com/stevenjwest/StereoMate). The Weka Workbench[16] training and testing machine learning classifiers.

Stereological Analysis: Synthetic Datasets

Images of systematically randomly placed objects were generated via an imagej macro by randomly allocating objects to a series of 128x128 pixel blocks. Objects were either squares (16x16, 32x32, 64x64), circles (diameters of 16, 32, 64), or lines of vertical, horizontal or diagonal orientations (4x 16, 32, 64). A sampling region measuring 1280x1280 was taken at random from a larger parent image, to ensure random sampling of the objects, and all objects were counted, rejecting any which touched the image edges. For the ROI DiSector, a larger sampling region was used, adding the maximum length of the object under assessment to each dimension. Analysis consistent of rejecting all objects which contacted the image edge, but also removing any objects which fall completely within the exclusion zone.

Manual simple and stereological Analysis of DRGs

Simple counts were performed in 3D, and every instance of a DRG neurone identified in a 9 slice (9um) thick Z stack was counted, with no application of a stereological correction.

DRG image stacks were re-sampled for stereological analysis by systematically deriving substacks 20 slices (20um) thick, taken every 10 slices. Only 9um were assessed per sample, allowing for the first slice as an initial look-up section, and the remaining 10 slices as an exclusion zone (to allow confirmation if new objects at the bottom of the stack were neuronal nuclei or not).

Both simple and stereological counts were performed on systematic random samples across 5 DRGs, derived at a sampling rate of 1/3 or 1/4. To derive a total neuronal number estimate, the DRG neurone number was multiplied by the sampling denominator.

Figures and Statistics

FIJI (Fiji Is Just ImageJ) was used for creating all image panels in figures. R and R Studio was used for all graphs and statistical assessments.

Results

The StereoMate Platform: Tissue Clearing and Immunofluroescence Labelling

The StereoMate platform consists of a set of tissue clearing and immunofluorescence labelling protocols, and an automated stereological image analysis framework. The first step was to develop an immunofluorescence labelling protocol suitable for thick or wholemount tissue specimens (Figure 1a). A key problem with previous tissue clearing methodologies is their impact on antibody affinity to their antigens[17,18], and so the first goal was to develop a methodology that removed lipid membrane barriers to enhance antibody penetration into tissue, yet still maintained tissue antigenicity.

A series of solvents utilised for lipid elution were tested for their ability to retain antigenicity, across antigens from different cellular structures (including cytosolic, cytoskeletal, nuclear and membrane), in mouse spinal cord. This revealed that across all antigens, using propanol as the lipid eluting solvent retained immunofluorescence signal (Figure 1b).

A second challenge with tissue clearing preparations is optical access, which can be resolved with refractive index (RI) matching. Lipid elution results in a tissue preparation largely composed of protein, which varies in refractive index from ~1.43 when hydrated to >1.5 when dehydrated[19,20]. As dehydrated protein closely matches the RI of borosilicate glass coverslips and immersion oil, and antibody-tagged fluorophores remain fluorescent in tissue after solvent dehydration and organic media mounting (unlike fluorescent proteins, see[21]), a design decision was made to exploit these features by dehydrating and mounting tissue in BABB (Figure 1a). This resulted in well matched RI throughout the light path, and thus eliminated RI variance as the Z stack was traversed. This allowed confocal imaging data to be acquired at high resolution and with minimal impact on signal strength throughout the Z stack (Figure 1c).

Thus, lipid elution with propanol provides antibody access to antigens for optimal tissue labelling, and RI matching during tissue mounting gives optical access throughout tissue blocks. Together these facilitate the generation of high quality 3D reconstructions of immunofluorescently labelled tissue elements.

The StereoMate Platform: Automated and Unbiased Image Analysis

The next challenge was to develop a framework for quantitative assessment of 3D datasets, in a demonstrably accurate and reliable manner. The StereoMate image analysis framework can assess biological objects using automated and stereological methods. This involves sketching regions of interest (ROIs) to define regions for object analysis (*ROI Sketcher plugin*), interactively establishing an image segmentation procedure to extract biological objects of interest from the raw image data (*Threshold Manager plugin*), and demonstrating the accuracy of this

segmentation procedure through assessment at the object level (*Object Manager plugin*). Finally, the image segmentation protocol is used to derive biological objects for automatic assessment in an ROI-dependent manner, using a novel stereological probe (*StereoMate Analysis plugin*).

User-defined ROIs can be optionally defined on input images with the ROI Sketcher Plugin, assigning biological objects to regions within the tissue. The StereoMate framework also optionally provides an Image Deconvolution plugin, with built-in PSFs, for use prior to image thresholding (*StereoMate Deconvolution plugin*), which improves image resolution and signal contrast with high resolution imaging.

The Threshold Manager Plugin plays the crucial role of defining a segmentation procedure. This is developed interactively by a user, by building a sequence of image processing operations. These operations act on the current image, and the user can decide visually when a suitably accurate segmentation operation is defined.

The accuracy of object segmentation underpins the quality of the object-level data extracted in the analysis step. It is therefore essential to demonstrate, on a sample of objects, the accuracy of this segmentation. The Object Manager Plugin facilitates this necessary step. The plugin displays both the raw pixel data, overlaid with an image segmentation procedure defined by the Threshold Manager. The user can generate sample selections of segmented objects to inspect their 3D characteristics and classify them.

Common segmentation problems include inaccurate object representations that do not fit to the underlying pixels, and the connection of independent objects during segmentation. These problems are overcome through sequentially optimising and assessing the segmentation procedure with the Threshold and Object Manager plugins.

The Object Manager further provides the ability to develop an object filter - to define a sub-group of biological objects for analysis. The object filter can be either a simple high- and low- pass filter on a single feature of the objects, or a machine learning classifier, applied to multiple features, trained by the user classification of a sample of objects.

Once object segmentation has been optimised, object-level data is extracted with the StereoMate Analysis Plugin. The assessment of objects from a tissue segment is subject to a range of biases, which can be eliminated through the use of stereological techniques (Figure 1d).

To overcome this bias in biologically relevant regions, the ROI Di-Sector was developed. This di-sector probe applies the logic of the optical di-sector (22, 23) to user defined ROIs of a 3D sample. The algorithm ensures an unbasied set of fully reconstructed objects are returned from each ROI, by replacing acceptance lines with exclusion zones (Figure 1d & 1e). Each object in the unbiased sample is measured for size, shape, location and intensity data.

The StereoMate Workflow provides robust histological labelling of thick tissue blocks for detailed reconstruction of labelled elements, and an image analysis workflow that delivers demonstrably accurate, reliable and deep object-level quantitative data for statistical analysis.

This method has been applied to both wholemount dorsal root ganglia (DRG) preparations to assess total neurone numbers in DRG, and to dorsal horn to assess primary afferent axonal input and synaptic puncta, presented next.

The StereoMate Workflow can effectively assess all neurones in wholemount Dorsal Root Ganglia:

The StereoMate workflow was applied to a wholemount dorsal root ganglion (DRG), to assess all neurones in this structure. The DRG provides a relatively small structure which can in theory be fully reconstructed to assess all neurones using tissue clearing methodology, which would demonstrate the benefits of this methodology over stereological estimates of neurone number.

As DRG neurones are densely packed, a strategy was devised to label neuronal nuclei, which are more easily resolved than neuronal soma labelling. TDP43 was identified from single cell transcriptomic data from DRG (24) as a highly expressed nuclear antigen across all DRG neurone sub-types. Labelling of TDP43 in wholemount DRGs revealed strong expression and localisation to neuronal nuclei (Figure 2a, Supplementary Video 1), but also within satellite glial and schwann cell nuclei. The nuclear labelling was well maintained both to the centre of the tissue, indicating sufficient penetration of antibody, and to the bottom of the Z stack, demonstrating good matching of refractive index throughout the light path.

To confirm TDP43 labelled all neuronal nuclei, a transgenic mouse where EGFP was expressed under the Advillin promotor (known to be expressed across the range of DRG neurones[25,26]) were co-labelled with anti-TDP43 and anti-EGFP antibodies (Figure 2b, Supplementary Video 2). In all tissue analysed, neuronal cell bodies showed varying levels of EGFP expression, and each EGFP+ neurone possessed a TDP43+ nucleus.

A nuclear object segmentation protocol was established with the Threshold Manager plugin and validated with the Object Manager plugin. It was found that optimal segmentation was achieved with a narrow confocal pinhole (0.5AU), application of a bandpass filter to suppress non-neuronal signal, and segmenting the histogram by fitting it to a multi-modal model (Figure 2c).

To separate the remaining glial nuclei from neuronal nuclei, a machine learning classifier was trained from a sample of user-classified TDP43+ nuclei (Figure 2D). This classifier showed robust performance (~99% accuracy) on a large independent test set (Supplementary Figure 8), providing high confidence in the quality of the classifier. The StereoMate Analyser plugin was then used to extract all objects classified as neuronal nuclei for analysis.

To explore the data, some basic plots were generated (Figure 2e-f). Adult mouse L4 DRGs were found to contain 8,677.6±809.9 (mean±SD; n=5) DRG neurones. A plot of the size histogram of DRG nuclei reveals a novel trimodal distribution. This is contrary to previous 2D analyses of DRG soma size, which reveal a bimodal distribution (27).

The StereoMate Workflow Improves on the Gold Standard Manual Stereological Assessment:

To validate the StereoMate methodology, wholemount DRG analysis was compared to the current Gold Standard method for unbiased object assessment: stereology. To enable a direct comparison between the StereoMate analysis and a manual stereological assessment, the confocal image stacks from a set of DRGs were digitally re-sampled to generate a set of systematically randomly sampled images (Figure 3a & 3b).

Both simple counts of 2D profiles of neuronal nuclei, where the total number of nuclear profiles in a section is counted and then multiplied by ganglion volume to generate a total number, and application of the Optical Fractionator stereological method, were performed on the DRG samples, at two sampling rates (1/3 and 1/4 of the total DRG volume, Figure 3c). Across all DRGs assessed, using simple counts resulted in a large over-estimate of neuronal numbers, a reflection of the fact that each nucleus is cut into multiple profiles and so will be 'double counted' using this methodology[11,12]. However, application of stereological technique corrected this to bring the estimate of neuronal numbers in each DRG to cluster around the actual count from 3D reconstruction, thus validating both the 3D reconstruction numbers and the stereological methodology.

Although the set of stereological estimates tends to cluster around the 3D reconstruction count value, any one estimate always deviates from the actual value. Therefore, the stereological estimate will always contribute extra variance to any statistical analysis of object counts.

To assess the degree of added noise imposed by a given analysis scheme, the coefficient of error (CE) was measured. The CE gives a measure of variation independent of the sample size and sample mean. Figure 3D shows a boxplot of the CE measured across all assessed DRGs, showing that CE tends to increase with reduced sampling. Interestingly, the CE is higher on average for stereological assessment than with simple counts, due to simple counts over-estimating the object number, but not increasing the variance by the same degree, which artifically brings down the CE. The key message, however, is that all the sampling schemes increase the variation seen in the estimates, compared to the 3D reconstructed counts, which contain no sampling error.

Comparisons were made in the time taken to assess each DRG. Although there is a significant overhead to set up the analysis whendefining and validating the segmentation procedure, the actual analysis per DRG is approximately 2 minutes.

Whereas, the manual assessments performed here sampling 1/3 of the DRG volume took approximately 4 hours of constant counting time per DRG.

Finally, a comparison was made between the resulting data. Whereas manual stereological analysis only yields a single estimate of an object measure (object number in this analysis), the StereoMate analysis platform yields an unbiased sample of objects which can be measured in various ways. This multivariate dataset allows a much wider variety of analyses to be performed across and between different object measures. It allows a greater sensitivity in detecting subtle changes, both through the increased sampling yielding lower variance in the total dataset, but also because of the greater number of measures made across the resultant object sample.

In conclusion, the StereoMate framework overcomes subtle biases present in manual stereological analysis, and delivers a richer dataset for more detailed analyses to be performed on.

The StereoMate Workflow Reveals a Profound DRG Neurone Loss following Peripheral Nerve Injury

To test the hypothesis that peripheral nerve injury results in a loss of DRG neurones, whole DRGs from 6 week post spared-nerve injury[14] (ipsilateral [L4i] and contralateral [L4c] L4 DRGs) and sham surgery (ipsilateral L4 DRGs only) was cleared and labelled for TDP43 (Figure 4a).

A segmentation procedure was developed with the Threshold Manager plugin identical to the previous procedure for naive tissue. Again optimal segmentation was achieved with a narrow confocal pinhole (0.5AU), application of a bandpass filter to suppress non-neuronal signal, and segmenting the histogram by fitting it to a multi-modal model.

A new machine learning classifier for this second dataset was trained from a sample of user-classified TDP43+ nuclei via the Object Manager plugin (Figure 4b). This classifier showed robust performance (~99% accuracy) on a large independent test set (n=1,000, accuracy 99.5%), providing high confidence in the quality of the new classifier. The StereoMate Analyser plugin was then used to extract all objects classified as neuronal nuclei for analysis.

Comparisons of total DRG neurone number between groups revealed a significant and profound reduction in DRG neurone number in the SNI injured DRGs (Figure 4c). An approximately 3/8 reduction in DRG neurone number is seen at this 6 week time point post nerve injury.

To identify which population(s) of neurones are lost at this timepoint, the size histograms were compared between groups. This revealed a significant reduction in the first two peaks of the size histogram, revealing an impact on small C fibres (Figure 4d).

Discussion

This work has developed and validated a new tissue clearing and image analysis platform, optimised for use with immunohistochemical interrogation of biological structures. The tissue clearing workflow offers improved antigenicity for a range of antigens tested, and delivers deep high resolution imaging with oil-immersion lenses, allowing detailed 3D reconstructions of immunofluorescently labelled structures of thick blocks of tissue. To effectively extract and analyse the labelled structures, the StereoMate image analysis pipeline provides tools for developing an object segmentation procedure, object sampling for assessment of object extraction quality and user-classification for machine learning training, and finally assessing objects in accordance with stereological principles.

This platform was applied to wholemount mouse DRGs, enabling full reconstruction of these structures. Assessing neuronal nuclei revealed relatively consistent DRG neuronal number for the L4 DRG, and a novel trimodal distribution of DRG neuronal nuclear size. Finally, clearing and labelling of DRGs 6 weeks post nerve injury revealed a ~3/5 loss of DRG neurones, exclusively from the smaller populations of the DRG.

Tissue clearing methodologies have had generated considerable interest since the landmark publication of the CLARITY methodology[2]. However, the uptake of these methods has been hampered by technical challenges, including achieving sufficient tissue clearing, adequate homogeneity of tissue refractive index for deep imaging, but most conspicuously for immunohistochemistry, retaining antigenicity.

The methodology presented here successfully overcomes these challenges to deliver a tissue clearing method suitable for quantitative assessment of immunofluorescently labelled structures. By using longer carbon chained solvents, which are routinely used for lipid extraction from tissues[28,29], antigenicity is well retained. This may be due to the higher lipophilicity allowing good lipid extraction while mitigating any impact on epitopes due to dehydration.

The standard tissue clearing mountant BABB[30] was used here, which offers good RI matching. The only way to guarantee a constant RI profile throughout the lightpath as the Z stack is traversed is by using a homogenous RI throughout. Therefore, oil-immersion lenses, borosilicate glass, and BABB-mounted tissue were used to guarantee a consistent RI was maintained in the lightpath throughout the Z stack. These two design choices guaranteed the highest resolution data even to great depth into the tissue, thus facilitating accurate quantitative analysis. An extra unexpected consequence of using organic media with fluorophores is the inability to bleach these specimens, which enables the use of this method with laser-scanning confocal microscopy.

Once data of sufficient quality for quantitative analysis has been acquired, a means of assessing this data which is automated and stereological becomes essential. The StereoMate platform delivers this in a general way, by providing the user with a

platform to design an image segmentation procedure interactively. This allows the user to develop a bespoke segementation protocol for the specific image analysis problem. However, a number of general principles have been found to help the user identify such a protocol.

First, applying a bandpass filter to the image in 3D to both enhance features of interest, and suppress signals in the data that mask features of interest, dramatically improves the quality of image segmentation. This requires some optimisation, but an adequate filter can often be developed in a small number of iterations. Second, immunofluroescent images contain multiple distributions of signal (including different fluroescence signal distributions outside of the tissue, tissue background fluroescence, variations with z-depth, and even different signal intensity distributions associated with different antigen densities throughout the tissue), and this often fits to a multi-modal histogram distribution. Although histogram segmentation procedures can be effective, the standard algorithms only fit a bi-modal model, which often results in a poor threshold selection for defining objects. A general principle which has been found to be very successful is to fit the histogram to a multi-modal model, and to then define the object-signal levels within this multi-modal distribution.

Although these setup procedures may seem arduous, and appear to take away from the automation promised by the StereoMate platform, ultimately, any automated system needs a human arbiter to decide what is correct. The StereoMate system allows the user to optimise their object segmentation procedure to the current problem, but furthermore enables this process to be quantitatively assessed through the Object Manager and user classification of the derived objects.

Integrating a stereological approach guarantees that any sampling of objects from tissue regions will deliver a sample that is unbiased, and therefore measurements made on this object sample will have distributions of properties that reflect the population of objects. The key advance of the StereoMate platform is moving from a stereological measurement to delivering a stereological sample, which can then be measured in various ways. The ROI DiSector delivers an unbiased sample of objects by employing the logic of the DiSector Probe[22] to image stacks. The consequence of requiring fully reconstructed objects from a sample is that larger objects are less likely to fall within the sample, and therefore be rejected in the analysis, which results in a bias in selecting smaller objects in 3D samples. By first rejecting all objects that are not fully reconstructed in the sample, and then removing objects solely in an Exclusion Zone along one half of the image stacks border, an unbiased sample of fully reconstructed objects is guaranteed to be delivered.

Together, the StereoMate platform delivers a histological workflow suitable for quantitative analysis of labelled tissue structures, and a software implementation that can extract objects from the pixel-level data, derive unbiased samples of these objects, and measure these in a multitude of ways for detailed quantitative analysis.

In this work, the StereoMate platform was applied to wholemount DRGs. This serves as an excellent demonstration of the benefits of tissue clearing, as whole DRGs can be reconstructed, enabling the whole population of DRG neurones to be assessed. Furthermore, the full reconstruction of a whole DRG has not been achieved, and quantitatively assessing all the neurones form DRGs would provide a wealth of data to help understand its 3D organisation.

This work has firstly identified the total number of DRG neurones in the L4 DRG to be around 8,000 in the mouse, consistent with previous stereological estimates[27]. It also identified a unique tri-modal distribution of DRG neuronal nuclei, contrary to previous reports of 2D DRG neuronal soma distribution[31]. The nucelar size does appear to correlate to the neuronal soma size, as can be appreciated from the TDP43 labelling in DRG.

The identification of a trimodal distribution is a result of the full reconstruction of DRG nuclei, as previous 2D size measurements are limited by the fact that only the area of a single z slice is measured, which will vary depending on where it cuts through the cell. The assumption this are will correlate to 3D volume is also not met. These factors result in a 2D distribution that hides the separate peaks in the C fibre size range.

Interestingly, an early report on DRG neurone size[31] suggests that different C fibres may have different size distributions, with the TH+ fibres showing a large peak in the small C fibre range, and IB4+ fibres showing an independent peak at a higher range. It is therefore likely the trimodal distribution seen here consists of a first TH+ peak, a second CGRP+/IB4+ peak, and finally a third and broader NF200+ (A fibre) peak.

Finally, DRGs were assessed after nerve injury, showing a profound loss of DRG neurones at 6 weeks post injury, and a significant shift in the size histogram. These data are consistent with the loss of C fibres at this timepoint, which has been previously demonstrated in the rat[32]. The DRG neurone loss is likely to be from IB4+ fibres, as it is known these fibres are sensitive to nerve injury: They lose their ability to bind IB4 and react to FRAP rapidly after injury, and their terminals show a delayed loss after injury, with the potential recovery with re-innervation[33,34].

The fact such a profound loss of cells is seen at relatively early time points after nerve injury has important implications for chronic pain patients. If nerve injury can result in large losses of DRG neurones in humans, and these populations cannot recover, it may contribute to chronicity of the neuropathic phenotype. Further work looking at the impact of re-innervation on DRG neurone number, and understanding how dorsal horn circuitry is altered by such a loss of neurones is necessary to fully understand the impact of this phenomenon.

Acknowledgements

We would like to acknowledge the Wellcome Trust and the Strategic Award "Defining pain circuitry in health and disease" for funding this research.

Figure Captions

Figure 1: The StereoMate Histological and Image Analysis Workflow. a, Thick blocks of nervous tissue are first fixed in formaldehyde solution (PFA) to crosslink protein, then incubated in buffered 1-propanol (1-PT) to elute lipids, and finally proteins of interested are labelled using standard immunofluorescence methods (Ab.). b, Using buffered solvent to elute lipids produces the most consistent signal for a range of common antigens in dorsal horn spinal cord (scale bar: 20um for Iba1 and NeuN, 10um for Syn1). c, Dehydration and buffered organic mounting in BABB-T results in good retention of fluorescence signal up to and beyond 200um Z-depth. d, The ROI Disector was tested with a synthetic dataset comprising systematically randomly distributed objects in 2D. This schematic illustrates an example the spheres_64 data, showing the application of the Exlcusion Zone to eliminate bias in object sampling. e, Boxplots of numbers obtained from systematically random distributions of objects of different size (16, 32, 64 pixel diameter), shape (sphere, cube, line), and orientation (line: vertical, horizontal, diagonal). All distributions were sampled with an area that should contain 100 objects on average. Dots represent samples of single pixels, and show no bias. Simple counts show progressively more bias (under-counting) with larger objects. Applying the ROI DiSector corrects this bias to identify object numbers around 100. 1-PT: 1-propanol + 0.3% TEA. MeDCM: Methanol-dichloromethane. Syn1: Synapsin 1.

Figure 2: Assessment of wholemount DRG neurones. a, Orthogonal Views of a cleared DRG labelled with TDP43 antibody, showing the XY and YZ views of the tissue block. Note the even labelling of TDP43+ nuclei to the centre and bottom (in Z) of the tissue block. b, Panel showing TDP43 and EGFP labelling in DRG indicating that TDP43 is expressed in all DRG neuronal nuclei. c, Overview of image filters applied prior to image segmentation. With the application of a low-pass filter (Median 3D) and a high-pass filter (High-Pass Gaussian filter 3d), it is possible to repress un-desired high- and low- frequency components, and therefore focus on extracting the desired neuronal nuclei, improving segmented object data quality. d, Scatterplot of segmented DRG objects showing the data distribution by size and sphericity measures. Each object has been classified by a KStar machine learning classifier as FEATURE (neuronal nucleus, green), NON-FEATURE (glial nucleus, red) or CONNECTED (two or more neuronal nuclei connected together, blue) The vast majority of objects are neuronal nuclei, due to image filtering. The decision boundary of the KStar classifier colours the scatterplot below the datapoints. e, Boxplot of DRG neuronal nuclear number, showing 8,677.6±809.9 (mean±SD; n=5) DRG neurones. f, Histogram of DRG neuronal nuclear size of all DRGs assessed (n=5). A trimodal distribution of neuronal nuclear size can be seen.

Figure 3: Comparison of StereoMate analysis to Manual Stereological analysis. a, Confocal image stacks of DRGs were re-sampled for manual stereological analysis using a systematic random sampling scheme. This schematic illustrates the sampling of one DRG to obtain a 1/3 fraction of the total DRG, according to the fractionator sampling rules. b, a single sample derived from a, projected to show the

typical TDP43 signal to be assessed stereologically. c, Boxplot showing the 3D counts, simple nuclear counts with 3x 1/3 and 4x 1/4 sampling (1/3 SC and 1/4 SC, respectively), and optical disector (fractionator) counts with 3x 1/3 and 4x 1/4 sampling (1/3 Fr. and 1/4 Fr. respectively). Simple counts over-estimate DRG neuronal number as predicted by stereological theory. Stereological analysis brings the estimate close to 3D object counts. d, The Coefficient of Error was measured for both simple and stereological counts. Quantification of whole DRGs (3D Counts) has no sampling error, as indicated. Simple and stereological counts have different sampling errors depending on the sampling and analysis scheme. Note, simple counts under-estimate the CE, due to an over-estimate of DRG neurone number without an equivalent increase in estimate error.

Figure 4: DRG neurones are lost following peripheral nerve injury. a, Example orthogonal views of DRGs labelled with TDP43 anti-antibody. The two DRGs are from the same sample, from the ipsilateral and contralateral L4 DRG. b, Scatterplot of segmented DRG objects from DRG images in (a), showing the data distribution by size and sphericity measures. Each object has been classified by a newly built KStar machine learning classifier as FEATURE (neuronal nucleus, green), NON-FEATURE (glial nucleus, red) or CONNECTED (two or more neuronal nuclei connected together, blue) The decision boundary of the KStar classifier colours the scatterplot below the datapoints. The cloud of FEATURE objects (neuronal nuclei, green) in the ipsilateral data appears to be significantly less than in the contralateral data. c, Boxplots of total DRG neuronal numbers for SNI L4i, L4c and SHAM L4i groups. Data compared using a t.test with adjusted p-values for multiple comparisons using the Holm method (****, $p<0.001$, n=6 for SNI groups, n=5 for SHAM group). e, Size histograms of summed DRG data, revealing a trimodal distribution for SNI L4c and SHAM L4i, but a large reduction in histogram size, and predominant loss of small DRG neurone populations in SNI L4i group.

References

1. Zukor, K. A., Kent, D. T. & Odelberg, S. J. Fluorescent whole-mount method for visualizing three-dimensional relationships in intact and regenerating adult newt spinal cords. *Developmental dynamics : an official publication of the American Association of Anatomists* **239**, 3048–57 (2010).

2. Chung, K. *et al.* Structural and molecular interrogation of intact biological systems. *Nature* **497**, 332–7 (2013).

3. Gleave, J. A., Lerch, J. P., Henkelman, R. M. & Nieman, B. J. A method for 3D immunostaining and optical imaging of the mouse brain demonstrated in neural progenitor cells. *PloS one* **8**, e72039 (2013).

4. Renier, N. *et al.* iDISCO: A Simple, Rapid Method to Immunolabel Large Tissue Samples for Volume Imaging. *Cell* **159**, 896–910 (2014).

5. Yang, B. *et al.* Single-Cell Phenotyping within Transparent Intact Tissue through Whole-Body Clearing. *Cell* **158**, 945–958 (2014).

6. Susaki, E. A. *et al.* Whole-brain imaging with single-cell resolution using chemical cocktails and computational analysis. *Cell* **157**, 726–39 (2014).

7. Schwarz, M. K. *et al.* Fluorescent-Protein Stabilization and High-Resolution Imaging of Cleared, Intact Mouse Brains. *PLOS ONE* **10**, e0124650 (2015).

8. Renier, N. *et al.* Mapping of Brain Activity by Automated Volume Analysis of Immediate Early Genes. *Cell* **165**, 1789–1802 (2016).

9. Murakami, T. C. *et al.* A three-dimensional single-cell-resolution whole-brain atlas using CUBIC-X expansion microscopy and tissue clearing. *Nature Neuroscience* **21**, 625–637 (2018).

10. Du, H., Hou, P., Zhang, W. & Li, Q. Advances in CLARITY based tissue clearing and imaging (Review). *Experimental and Therapeutic Medicine* **16**, 1567–1576 (2018).

11. West, M. J. Stereological methods for estimating the total number of neurons and synapses: issues of precision and bias. *Trends in neurosciences* **22**, 51–61 (1999).

12. Schmitz, C. & Hof, P. R. Design-based stereology in neuroscience. *Neuroscience* **130**, 813–31 (2005).

13. West, S. J., Bannister, K., Dickenson, A. H. & Bennett, D. L. Circuitry and plasticity of the dorsal horn - Toward a better understanding of neuropathic pain. *Neuroscience* **300**, 254–75 (2015).

14. Decosterd, I. & Woolf, C. J. Spared nerve injury: an animal model of persistent peripheral neuropathic pain. *Pain* **87**, 149–58 (2000).

15. Pichugin, Y., Fahy, G. M. & Morin, R. Cryopreservation of rat hippocampal slices by vitrification. *Cryobiology* **52**, 228–240 (2006).

16. Hall, M. *et al.* The WEKA Data Mining Software: An Update. *SIGKDD Explorations* **11**, (2009).

17. Susaki, E. A. & Ueda, H. R. Whole-body and Whole-Organ Clearing and Imaging Techniques with Single-Cell Resolution: Toward Organism-Level Systems Biology in Mammals. *Cell Chemical Biology* **23**, 137–157 (2016).

18. Xu, N. *et al.* Fast free-of-acrylamide clearing tissue (FACT)—an optimized new protocol for rapid, high-resolution imaging of three-dimensional brain tissue. *Scientific Reports* **7**, 9895 (2017).

19. Tuchin, V. V. Tissue Optics and Photonics: Light-Tissue Interaction. *Journal of Biomedical Photonics & Engineering* **1**, 98–134 (2015).

20. Seo, J., Choe, M. & Kim, S.-Y. Clearing and Labeling Techniques for Large-Scale Biological Tissues. *Molecules and Cells* **39**, 439–446 (2016).

21. Espada, J. *et al.* Non-aqueous permanent mounting for immunofluorescence microscopy. *Histochemistry and Cell Biology* **123**, 329–334 (2005).

22. Sterio, D. C. The unbiased estimation of number and sizes of arbitrary particles using the disector. *Journal of microscopy* **134**, 127–36 (1984).

23. Mayhew, T. M. & Gundersen, H. J. If you assume, you can make an ass out of u and me': a decade of the disector for stereological counting of particles in 3D space. *Journal of anatomy* **188 (Pt 1**, 1–15 (1996).

24. Usoskin, D. *et al.* Unbiased classification of sensory neuron types by large-scale single-cell RNA sequencing. *Nature Neuroscience* **18**, 145–53 (2014).

25. Ravenall, S. J., Gavazzi, I., Wood, J. N. & Akopian, A. N. A peripheral nervous system actin-binding protein regulates neurite outgrowth. *The European journal of neuroscience* **15**, 281–90 (2002).

26. Hunter, D. V. *et al.* Advillin Is Expressed in All Adult Neural Crest-Derived Neurons. *eneuro* **5**, ENEURO.0077–18.2018 (2018).

27. Lawson, S. N. The postnatal development of large light and small dark neurons in mouse dorsal root ganglia: a statistical analysis of cell numbers and size. *Journal of neurocytology* **8**, 275–94 (1979).

28. Guckert, J. B. & White, D. C. Evaluation of a hexane/isopropanol lipid solvent system for analysis of bacterial analysis of bacterial phospholipids and application to chloroform-soluble Nuclepore (polycarbonate) membranes with retained bacteria. *Journal of Microbiological Methods* **8**, 131–137 (1988).

29. Ferraz, T., Fiúza, M., Santos, M. dos, Pontes de Carvalho, L. & Soares, N. Comparison of six methods for the extraction of lipids from serum in terms of effectiveness and protein preservation. *Journal of Biochemical and Biophysical Methods* **58**, 187–193 (2004).

30. Zucker, R. M., Hunter, E. S. & Rogers, J. M. Confocal laser scanning microscopy of morphology and apoptosis in organogenesis-stage mouse embryos. *Methods in molecular biology (Clifton, N.J.)* **135**, 191–202 (2000).

31. Price, J. An immunohistochemical and quantitative examination of dorsal root ganglion neuronal subpopulations. *The Journal of neuroscience : the official journal of the Society for Neuroscience* **5**, 2051–9 (1985).

32. Tandrup, T., Woolf, C. J. & Coggeshall, R. E. Delayed loss of small dorsal root ganglion cells after transection of the rat sciatic nerve. *The Journal of comparative neurology* **422**, 172–80 (2000).

33. Csillik, B. & Knyihár-Csillik, E. Regenerative synaptoneogenesis in the Mammalian spinal cord: dynamics of synaptochemical restoration in the Rolando

Substance after transganglionic degenerative atrophy. *Journal of neural transmission* **52**, 303–17 (1981).

34. Bailey, A. L. & Ribeiro-da-Silva, A. Transient loss of terminals from non-peptidergic nociceptive fibers in the substantia gelatinosa of spinal cord following chronic constriction injury of the sciatic nerve. *Neuroscience* **138**, 675–90 (2006).

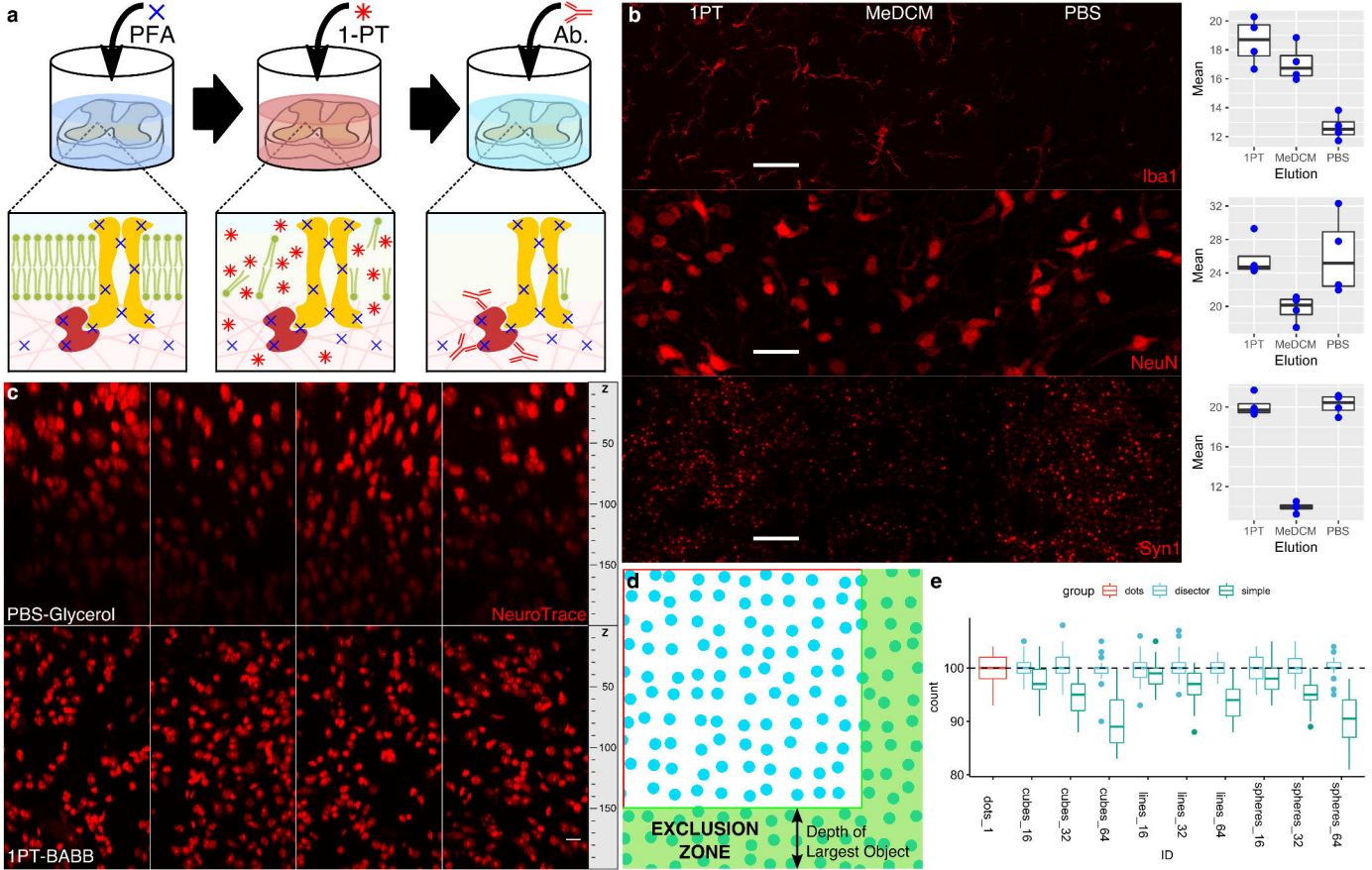
a
PFA
1-PT
Ab.
b
1PT
MeDCM
PBS
Iba1
NeuN
Syn1
Mean
Elution
c
PBS-Glycerol
NeuroTrace
1PT-BABB
z
d
EXCLUSION ZONE
Depth of Largest Object
e
group
dots
disector
simple
count
ID
dots_1
cubes_16
cubes_32
cubes_64
lines_16
lines_32
lines_64
spheres_16
spheres_32
spheres_64

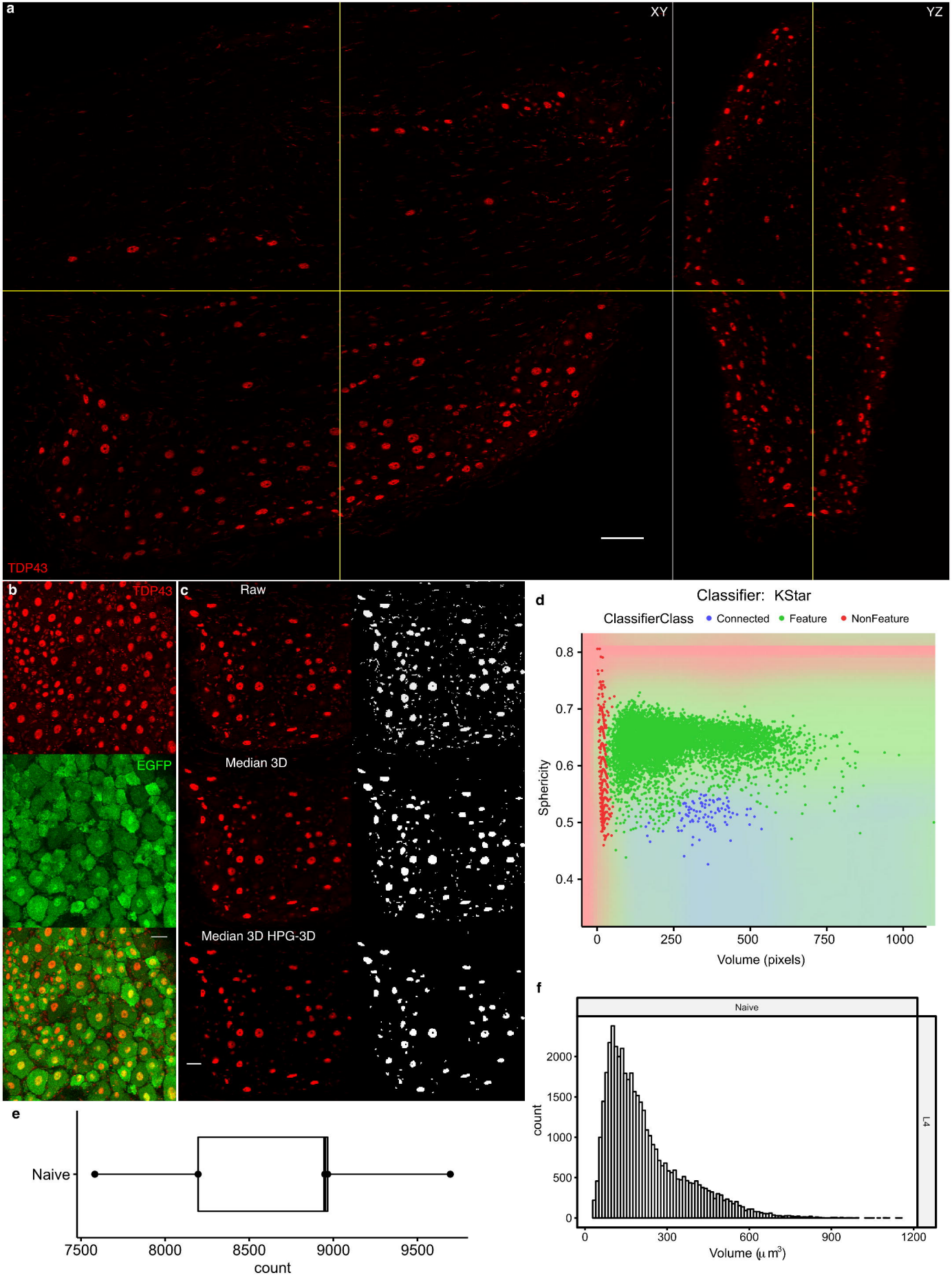
a
XY
YZ
TDP43
b
TDP43
EGFP
c
Raw
Median 3D
Median 3D HPG-3D
d
Classifier: KStar
ClassifierClass
Connected
Feature
NonFeature
Sphericity
0.8
0.7
0.6
0.5
0.4
0
250
500
750
1000
Volume (pixels)
e
Naive
7500
8000
8500
9000
9500
count
f
Naive
L4
count
2000
1500
1000
500
0
0
300
600
900
1200
Volume (μm³)

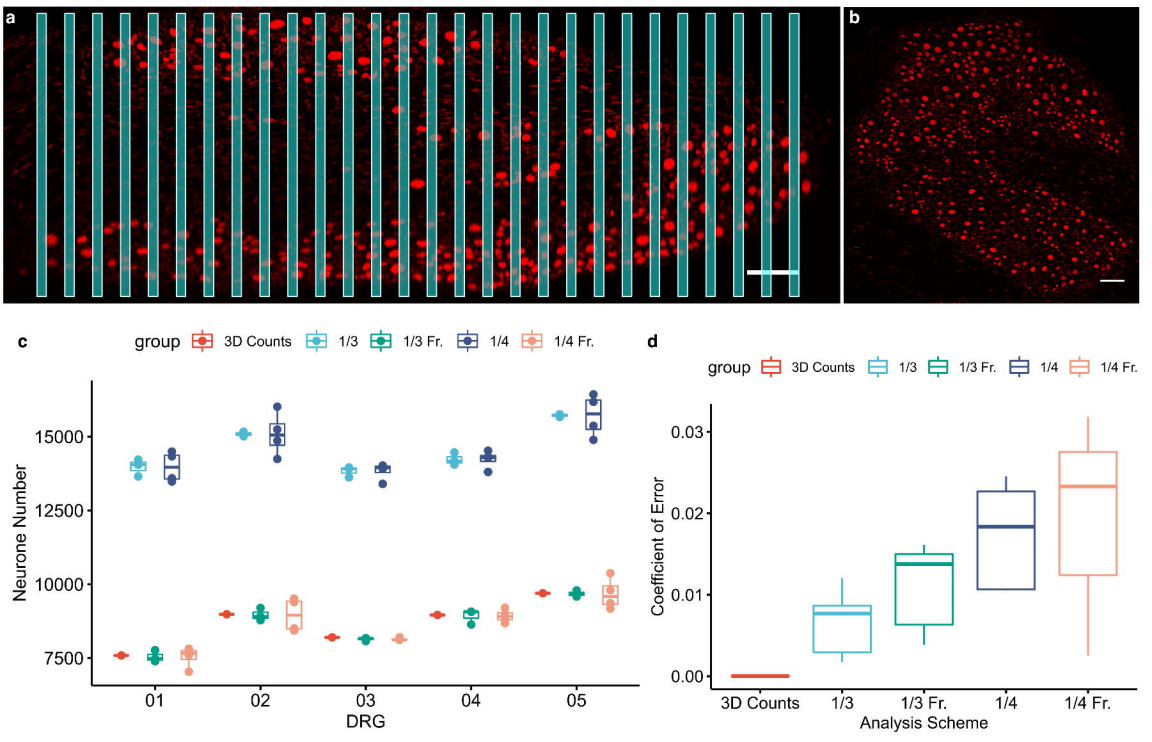
a
b
c
group
3D Counts
1/3
1/3 Fr.
1/4
1/4 Fr.
Neurone Number
15000
12500
10000
7500
01
02
03
04
05
DRG
d
group
3D Counts
1/3
1/3 Fr.
1/4
1/4 Fr.
Coefficient of Error
0.03
0.02
0.01
0.00
3D Counts
1/3
1/3 Fr.
1/4
1/4 Fr.
Analysis Scheme

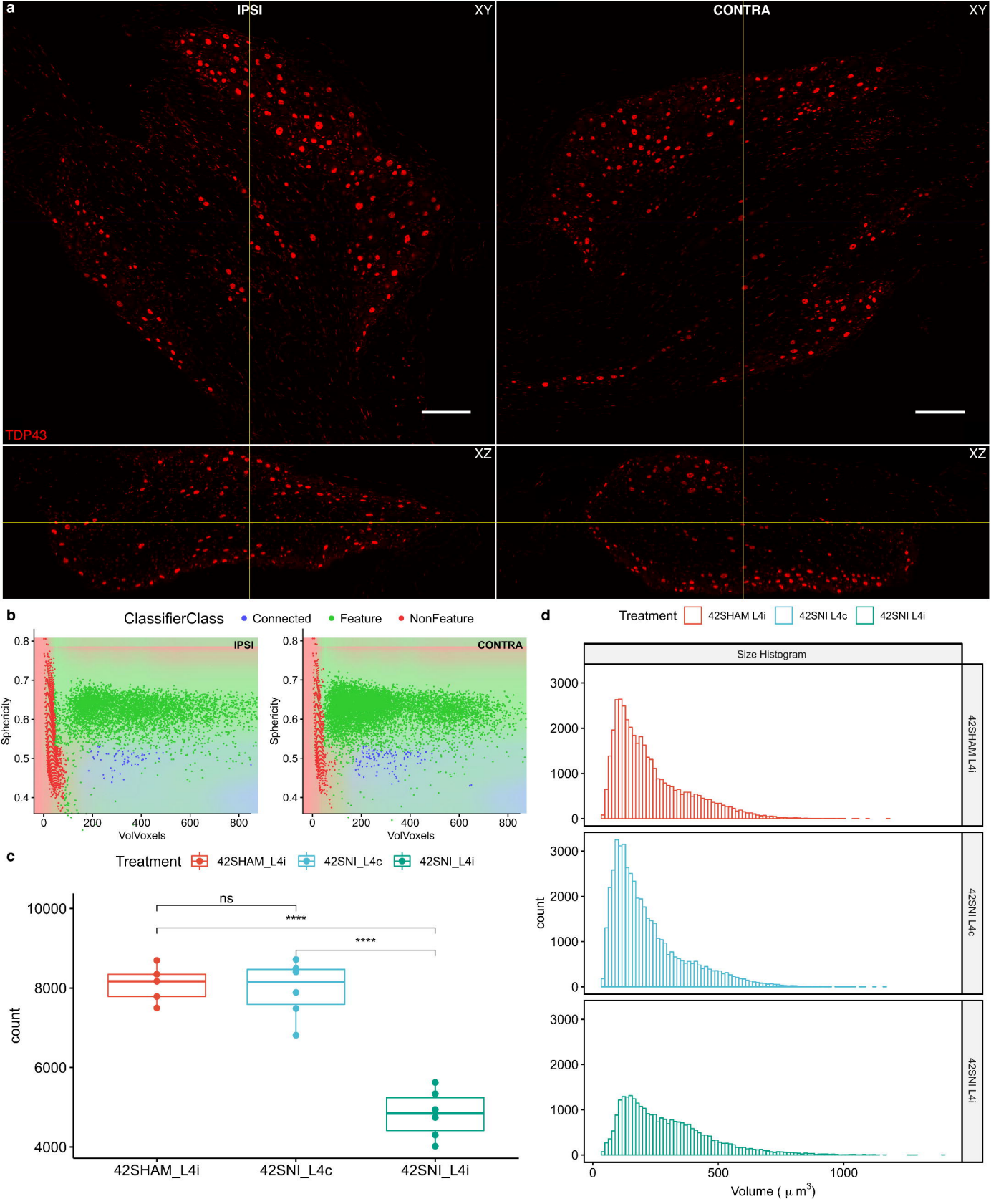
a
IPSI
XY
CONTRA
XY
TDP43
XZ
XZ
b
ClassifierClass
Connected
Feature
NonFeature
IPSI
CONTRA
Sphericity
VolVoxels
c
Treatment
42SHAM_L4i
42SNI_L4c
42SNI_L4i
ns
****
****
count
d
Treatment
42SHAM L4i
42SNI L4c
42SNI L4i
Size Histogram
count
Volume (μ m3)